## Nanoparticle Solar Cell Final Technical Report

### Executive Summary

The purpose of this work was to demonstrate all-inorganic nanoparticle-based solar cells with photovoltaic performance extending into the near-IR region of the solar spectrum as a pathway towards improving power conversion efficiencies. The field of all-inorganic nanoparticle-based solar cells is very new, with only one literature publication in the prior to our project. Very little is understood regarding how these devices function.

Inorganic solar cells with IR performance have previously been fabricated using traditional methods such as physical vapor deposition and sputtering, and solution-processed devices utilizing IR-absorbing organic polymers have been investigated. The solution-based deposition of nanoparticles offers the potential of a low-cost manufacturing process combined with the ability to tune the chemical synthesis and material properties to control the device properties.

This work, in collaboration with the Sue Carter research group at the University of California, Santa Cruz, has greatly expanded the knowledge base in this field, exploring multiple material systems and several key areas of device physics including temperature, bandgap and electrode device behavior dependence, material morphological behavior, and the role of buffer layers. One publication has been accepted to Solar Energy Materials and Solar Cells pending minor revision and another two papers are being written now.

While device performance in the near-IR did not reach the level anticipated at the beginning of this grant, we did observe one of the highest near-IR efficiencies for a nanoparticle-based solar cell device to date. We also identified several key parameters of importance for improving both near-IR performance and nanoparticle solar cells in general, and demonstrated multiple pathways which showed promise for future commercialization with further research.

### Overview

The goal of this grant was to demonstrate all-inorganic nanoparticle-based solar cells with photovoltaic performance extending into the near-IR region of the solar spectrum as a pathway towards improving power conversion efficiencies. Inorganic solar cells with IR performance have previously been fabricated using traditional methods such as physical vapor deposition and sputtering, and solution-processed devices utilizing IR-absorbing organic polymers have been investigated elsewhere, but a solution-processed all-inorganic nanoparticle solar cell with IR performance had not yet been demonstrated.

The solution-based deposition of nanoparticles offers a low-cost manufacturing method with the ability to tune the chemical synthesis and material properties to control the device properties.

The goal for this Phase I STTR grant was to demonstrate a power conversion efficiency of $\eta=1\%$ in the wavelength region above $\lambda=750nm$ in a nanoparticle-based all-inorganic solar cell. While our results were not as high as initially anticipated, we did demonstrate some of the highest near-IR efficiencies for nanoparticle-based devices to date. We also learned a great deal about the functionality and material requirements for nanoparticle IR solar cells and demonstrated pathways towards potentially successful results with further research and development. We also greatly advanced knowledge and understanding in the newborn field of all-inorganic nanoparticle solar cells, which prior to this consisted of a single publication in the literature. Towards that end, one journal article co-authored with our collaborators at UC Santa Cruz has been submitted for publication in Solar Energy Materials and Solar Cells (SolMAT) and another two articles are in the process of being written.

The following report summarizes the material and device approaches used in this research and the knowledge and insight gained during the course of this grant. We investigated a wide variety of approaches for producing nanoparticle solar cells with performance in the near-IR above $\lambda=750nm$, utilizing both bulk and quantum-confined properties of the IR-absorbing materials PbSe, HgTe and CdHgTe. An overview of the research approaches is summarized in Figure 1. We also studied CdTe nanoparticle devices to both further understanding of nanoparticle solar cell physics and as a framework for later application in CdHgTe near-IR devices.
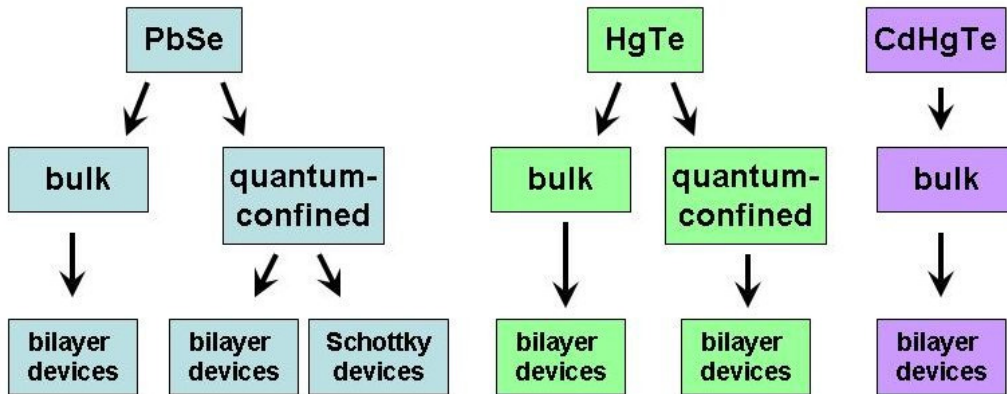


Figure 1: An overview of the materials and device approaches utilized over the course of the grant.

## Material Synthesis

### PbSe nanoparticles

PbSe nanoparticles were synthesized via a colloidal synthesis. In a typical reaction, 20 mmol (4.4 g) lead oxide (PbO), 20 ml oleic acid, and 20 ml trioctylamine are mixed in a three necked flask and heated under alternate vacuum and argon purge at 180C for 30-40 minutes. By this point, the reaction mixture turn has turned into a clear

and colorless single phase solution. A needle is then inserted through the septum to let moisture and vapor-phase side products escape. The needle is removed after about 30 min and the temperature is brought down to 155 C.

Meanwhile, 3.2 g Se is dissolved in 20 ml tributylphosphine (TBP-Se, 2M) inside the glove box and loaded into a syringe. 400 μl diphenylphosphine (DPP) is loaded into another syringe. These syringes are brought outside the glovebox and the contents of both are injected into the reaction pot simultaneously. The size of the particles is determined by the reaction time; for this work, a typical reaction time of 110-120 seconds was used to produce particles of ~ 4 nm corresponding to a highest excitonic peak of ~1500 nm. Shorter reaction times, down to 10-20 seconds, can be used to produce smaller particles. Heating is ceased by lowering the heating mantle and the reaction is stopped by quickly cooling the flask either by injecting ~50 ml trioctylamine or by bringing a chilled bath underneath the flask.

The product mixture is transferred by a cannula to an argon filled bottle and transferred into the glove box. Dry ethanol (~150-200 ml) is added to the mixture, which is first vortexed for 5-7 minutes and then centrifuged at 3200 rpm for ten minutes. The supernatant is clear and is discarded. The precipitate is redissolved in 50 ml toluene and mixed with 150 ml ethanol for a second centrifugation of ten minutes. The second precipitate is dissolved in 8-10 ml chloroform and filtered through a 0.2 μm membrane filter to remove any large particle aggregates.

The PbSe particles were characterized by solution absorption (Figure 2A), TEM (Figure 2B) and thermogravimetric analysis (TGA).
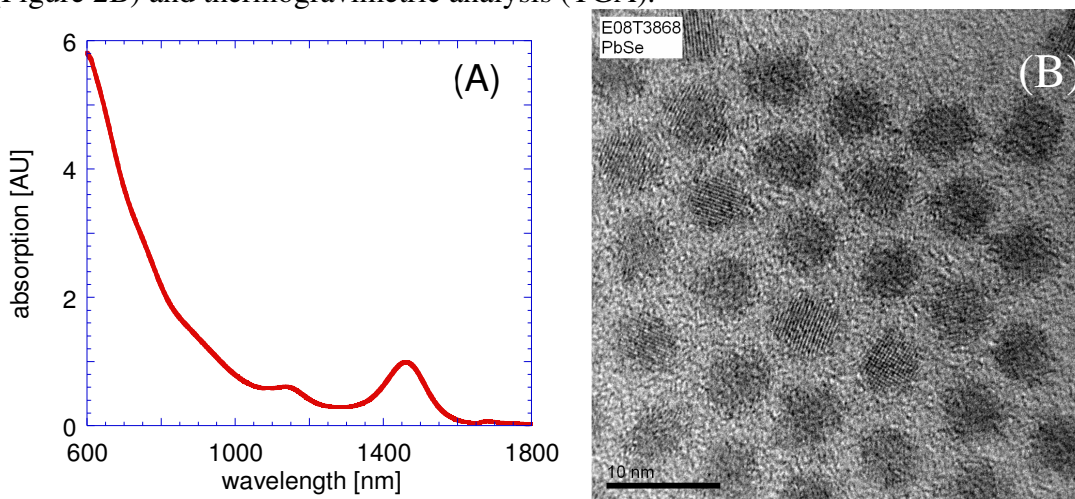


Figure 2: (A) PbSe solution absorption spectra; (B) a TEM image of the PbSe particles used in the quantum-confined device work described below.

## $Cd_xHg_{1-x}Te$ nanoparticles

$Cd_xHg_{1-x}Te$ nanoparticles are synthesized in an aqueous solution and subsequently transferred to an organic phase. In a typical reaction for $Cd_xHg_{1-x}Te$ with a target of x=60% (40% Hg), 3.11 g cadmium perchlorate $(Cd(ClO_4)_2 \cdot x\ H_2O$, FW=311.11), 2 ml thioglycerol and enough NaOH to maintain the pH at 11-12 are dissolved in 500 ml water in a flask and deaerated for ~15 mins on an ice bath (Flask 1). In a separate flask,

1.6 g mercury perchlorate ($Hg(ClO_4)_2 \cdot x \ H_2O$, FW=399.49), 50 ml water, 1 ml thioglycerol and enough NaOH to maintain pH at 11-12 are mixed (Flask 2).

In a 40 ml vial, 2 g aluminum telluride is placed and sealed by a septum fitted with a hard rubber pipe to pass $H_2Te$ gas. The other end of the pipe is immersed in the Flask 1. 1 ml $H_2SO_4$ is diluted to 5 ml and loaded into a syringe. The acid is dropped into the aluminum telluride while keeping the vial in ice bath. The resulting product, $H_2Te$ gas, is bubbled into Flask 1 and orange coloration appears indicating the formation of CdTe dots.

In later experiments, we explored the use of the Te precursor NaHTe in place of $H_2Te$ gas. 0.64 g (0.5 mmole) tellurium powder is weighed inside the glove box and placed in a closed vial fitted with a septum before being brought outside of the glovebox. 20 ml water and 12 mmole sodium borohydride are added and Ar flushed continuously for two hours. By this point, all the tellurium powder has dissolved and the color of the solution is light pink. This product is NaHTe (0.5 mmole in 20 ml) and can be stoichiometrically used for the preparation of either $Cd_xHg_{1-x}Te$ or HgTe.

Following this the content of Flask 2 is slowly poured into Flask 1. The solution color instantly turns dark, indicating the binding of Hg ions to the CdTe particles. The resulting product ($Cd_xHg_{1-x}Te$) is precipitated from the aqueous dispersion by adding excess acetone ( aqueous: acetone ratio 1:5) and centrifuging. The $Cd_xHg_{1-x}Te$ particles are easily re-dispersed in water (~20 ml).

In order to transfer the particles from aqueous to organic solution, 20 ml $Cd_xHg_{1-x}Te$ solution is mixed with 20 ml dodecanethiol (DDT) and 60 ml acetone. This mixture is heated at 70C for 1-2 hours, during which time the particles transfer to the organic DDT layer. The particles are precipitated from the organic layer by adding acetone and redispersed in chloroform for two cycles. The final solution is passed through a 0.2 µm membrane filter.

The $Cd_xHg_{1-x}Te$ particles were characterized by absorption spectra (Figure 3), energy dispersive spectroscopy (EDS) and direct coupled plasma (DCP), the latter two measurements used to determine the degree of Hg incorporation. Feedback from these measurements, showing a higher Hg inclusion than anticipated, guided later synthesis batches to tune the Hg content.
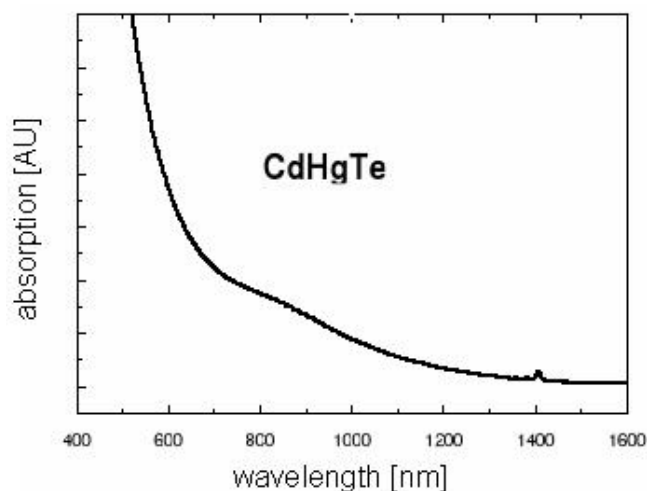


Figure 3: Solution absorption spectra for one example of CdHgTe nanoparticles.

**HgTe nanoparticles**

HgTe particles are prepared by passing $H_2Te$ gas into a mercuric perchlorate only solution (no cadmium perchlorate) in conditions otherwise identical to the preparation of described above for $Cd_xHg_{1-x}Te$. The phase transfer is achieved by the same procedure as described above.
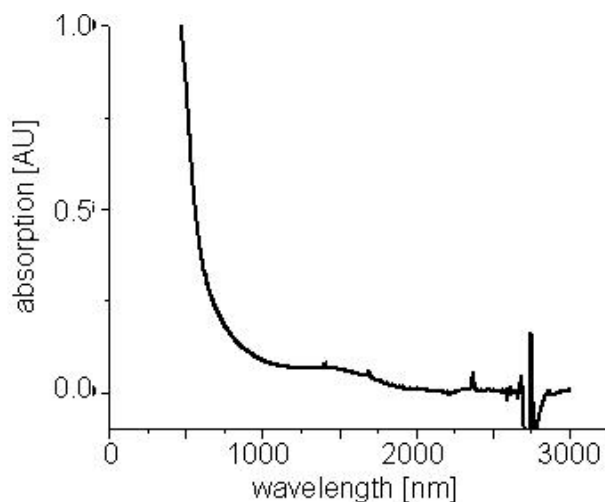


Figure 4: HgTe nanoparticle solution absorption spectrum.

**CdTe nanorods**

In a typical reaction, 4g cadmium oxide (CdO), 16.2 g octadecylphosphonic acid (ODPA), 6.2 g octyl phosphonic acid (OPA) and 53 g trioctylphosphonic oxide (TOPO, 99%) are loaded in a three necked flask and heated under alternate vacuum and argon purge for an hour at a set temperature of 320C, by which point the reaction mixture has formed a homogeneous clear solution. 30 ml trioctylphosphine (TOP, 98%) is introduced to the mixture and the heating continued for an additional 30 minutes. Next, 24 ml 1M TOP-Te (tellurium dissolved in TOP at a concentration of 1M) is rapidly injected, resulting in a brown solution indicative of the formation of CdTe nanorods (NRs). The reaction is stopped after 4 minutes by withdrawing the heating mantle. After the flask has cooled to a temperature of 80-100C, ~50 ml toluene is mixed with the product and the entire content of the flask is taken inside the glove box where it is mixed with 2-propanol (until slight cloudiness appears) and transferred into centrifuge tubes for precipitation and redispersion cycles.

For sintered device fabrication, it is advantageous to utilize ligands which can be removed by thermal annealing at moderate rather than high temperatures. For this reason, the CdTe NRs are surface exchanged with the more easily removable ligand pyridine. For simplicity, pyridine is used as the solvent as well. For this, the final precipitate from above (i.e. after centrifugation with 2-propanol) is transferred to a 3-neck flask and 700

ml pyridine added. The NR suspension in pyridine is subjected to 20-24 hour refluxing under argon after which it forms a clear dispersion in pyridine. The phosphonic acid ligands replaced by pyridine are still in the solvent, and need to be removed. This is done by precipitating the NRs from the pyridine dispersion by adding excess hexane and redissolving the precipitate in pyridine. A final concentration of 60-70 mg/ml is used to produce high quality uniform films.
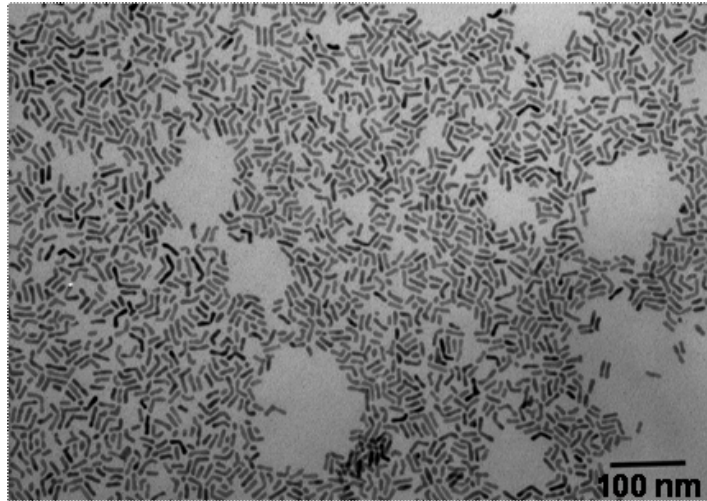


Figure 5: TEM image of CdTe nanorods.

**CdSe nanorods**

The preparation of CdSe NRs is very similar to the above description for CdTe. In a routine synthesis, 4.10 g CdO, 14.2 g tetradecylphosphonic acid (TDPA), 3.20 g hexylphosphonic acid (HPA) and 60 g TOPO are heated together to a temperature of 300C under the aforementioned conditions. 30 ml TOP is added and the heating continued for 30 minutes more. 10 ml 1M TOP-Se (selenium dissolved in TOP) is rapidly injected producing NRs of CdSe. The precipitation-redispersion cycle and the final pyridine dispersion are identical to the one described for CdTe NRs.
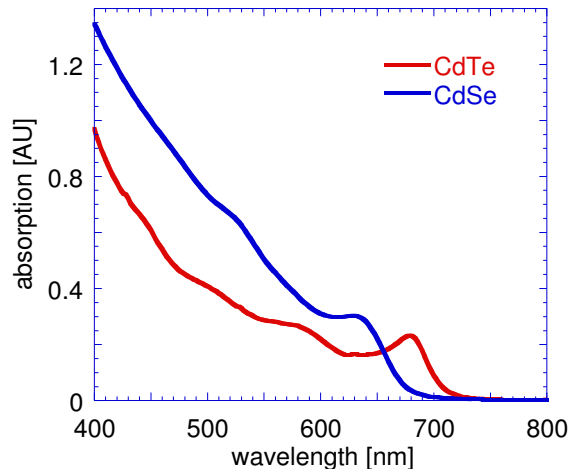
Figure 6: CdTe and CdSe nanorod solution absorption spectra.

**CdSe nanoparticles**

CdSe nanoparticles, rather than CdSe NRs, were used for some of the early work for this grant. In a routine synthesis, 3.45 g  cadmium carbonate ($CdCO_3$), 14.12 g oleic acid and 75 ml trioctylamine are taken in a three necked flask. Under alternate argon and vacuum, the flask is heated at 280C for 30 minutes. The heating is continued for another 30 minutes under argon with a needle pierced through the septum to let vaporized side products escape. 10 ml 1M TBP-Se (selenium dissolved in tributylphosphine) is rapidly injected by a syringe and the heating continued for an additional 30 minutes.  The CdSe QDs formed are retrieved by the established washing procedure discussed earlier for NRs. The QDs are dispersed in chloroform or dichlorobenzene.

## *Device Fabrication and Results*

**PbSe sintered nanoparticle solar cells**

We initially studied PbSe solar cells as an attempt to improve absorption and quantum efficiency in the IR portion of the solar spectrum. Our strategy was to replace the CdTe p-type layer with a PbSe p-type layer, following a similar device structure originally proposed by Gur et al.  For these CdSe/PbSe devices, we found that an additional buffer layer, such as LiF or $Al_2O_3$, was needed to obtain reproducible solar cell performance. We fabricated unoptimized solar cells with a short-circuit current of 6 mA/cm$^2$, an open-circuit voltage of 0.18 V, and a fill factor of 41%.  The PbSe in these devices did not contribute to the quantum efficiency even though it was a necessary component to make a working solar cell.  We concluded the solar cell did not behave as either a typical p-n or type-II heterojunction donor/acceptor.  A paper on these results was submitted to *Solar Energy Materials and Solar Cells* and has now been accepted for publication pending minor revisions.

The CdSe/PbSe devices were fabricated on ITO-patterned glass by Thin Film Devices (Anaheim, CA) which were cleaned by successively introducing the substrates into a sonic bath in an Alconox/deionized water solution, ethanol, and finally acetone, and then dried with a nitrogen gun. CdSe nanoparticle solution was spin-cast at 1000 rpm and then sintered at $400^oC$ for 10 min in air. CdSe film thickness ranged from 240 nm to 550 nm, depending on the concentration of the nanoparticle solution. A film of LiF was then thermally evaporated on the CdSe layer, and this was followed by a film of PbSe nanoparticles, also spun at 1000 rpm and sintered at $400^oC$ for 10 min in air. PbSe film thickness ranged from 90 nm to 340 nm. The nanoparticle films were sintered by introducing the substrates in a tube furnace at setpoint temperature; this was required to obtain short circuit currents above 0.1 mA/cm$^2$. Finally, Al or Au were thermally evaporated as the top metal electrode. Interlayers of $Al_2O_3$ were obtained by thermally evaporating a thin Al film over the CdSe layer, and then sintering at $400^oC$ for 2 min in air.

Figure 7a shows the IV characteristics for a typical ITO/CdSe/PbSe/Al device and an ITO/CdSe/LiF(34nm)/PbSe/Al device. The device without an interlayer shows severe shunting, high dark current, and no photovoltage or photocurrent. Incorporating an interlayer into the structure lowers the dark current and produces a photocurrent and a photovoltage under illumination. The dependence of device performance on LiF interlayer thickness is shown in Fig. 7b. The variability in nanoparticle solution and subsequent film quality led to variable optimal LiF film thickness; a trend was observed, however, whereby devices showed enhanced performance for thicknesses up to around 45 nm and performance decline starting around 50nm. We have observed that in general thicker nanoparticle films (up to 500 nm for CdSe films) resulted in higher performance devices. The IV characteristics of devices with optimized LiF thickness were: $J_{sc}$ of 6 mA/cm$^2$, $V_{oc}$ of 0.18V, and FF of 41%. The shunt resistance of ITO/CdSe/LiF/PbSe/Al devices monotonically increased with LiF layer thickness. This was consistent with the observation that introduction of an interlayer generally lowered the dark
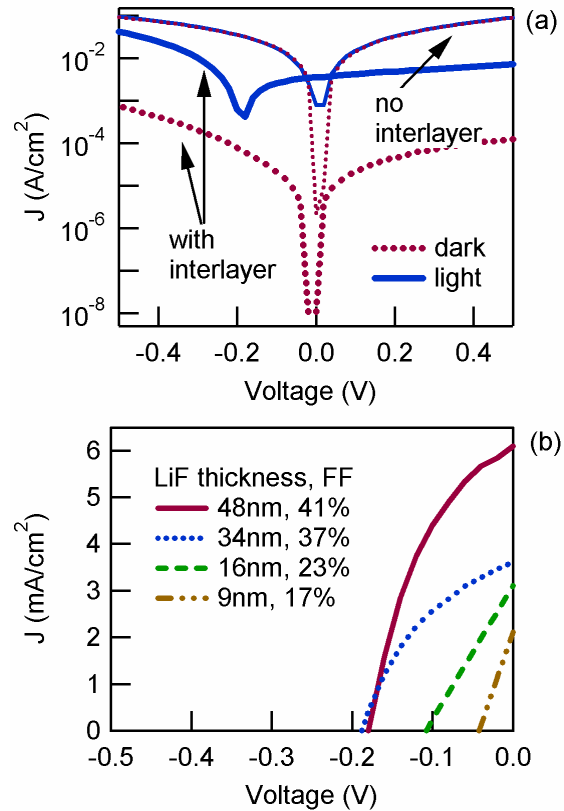


Figure 7: (a) Comparison of device performance in the dark (thin lines) and under AM1.5D illumination (thick lines) of ITO/CdSe/(LiF)/PbSe/Al devices, with and without a LiF interlayer. (b) Dependence of device performance on LiF interlayer thickness.

current of the devices.

To further understand the function of the interlayer, we replaced LiF with $Al_2O_3$ (Figure 8). These devices showed similar behavior to the LiF interlayer counterparts, although 20 nm of $Al_2O_3$ were sufficient to achieve IV characteristics similar to those of a device with a 50 nm LiF interlayer. We attribute the difference in thicknesses to the small but non-negligible conductivity of the LiF layer. By thermally evaporating a LiF film and an Al electrode on an ITO substrate and then measuring the IV curve of the structure, we verified that the LiF films exhibited a conductivity of $10^{-7}$ S/cm. We



Figure 8: Comparison of $Al_2O_3$ (20nm) and LiF (50nm) interlayer devices.

also tested the effect of introducing a thick, 30 nm LiF interlayer into a poly[2,5-dimethoxy-1,4-phenylene-1,2-ethenylene-2-methoxy-5-(2-ethylhexyloxy)-1,4-phenylene-1,2-ethenylene]/poly[oxa-1,4-phenylene-1,2-(1-cyano)-ethenylene-2,5-dioctyloxy-1,4-phenylene-1,2-(2-cyano)-ethenylene-1,4-phenylene] (M3EH-PPV/CN-ether-PPV) polymer bilayer system, which has been well studied by our group in the past [29].

Devices prepared with a 30 nm thick LiF interlayer resulted in a $J_{sc}$ of less than $1\mu A/cm^2$, over a two order of magnitude decrease, as well as a greatly reduced $V_{oc}$ of less than 0.05V. For the polymer devices, the LiF layer acts as an impediment to charge transfer and transport.

AFM images (Figure 9) showed that the CdSe films had a root-mean-square roughness ($R_{rms}$) of less than 5 nm and the PbSe films presented an $R_{rms}$ of up to 16 nm. In general we were not able to resolve any aggregates in the CdSe AFM images, while sintered PbSe nanoparticle aggregates exhibited diameters of the order of 0.50-0.75 $\mu$m. Inspection of the as-cast films revealed that the extent of aggregation and the size of the aggregates in the sintered film depended more heavily on aggregation in the nanoparticle solutions than on the sintering process. The CdSe films that resulted in the best devices had an $R_{rms}$ of around 2 nm, and in general we observed that obtaining very smooth nanoparticle films was crucial to fabricate the highest efficiency solar cells. We also observed that, in general, thicker nanoparticle films (up to 500 nm for CdSe films) resulted in higher performance
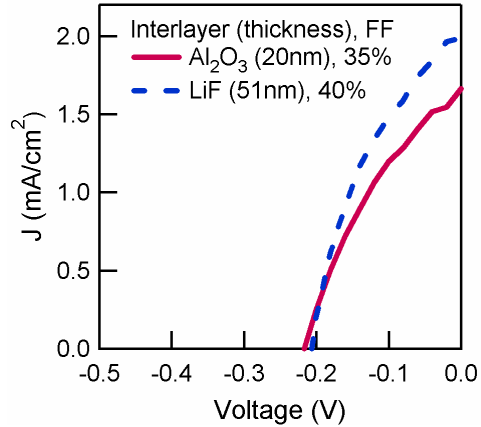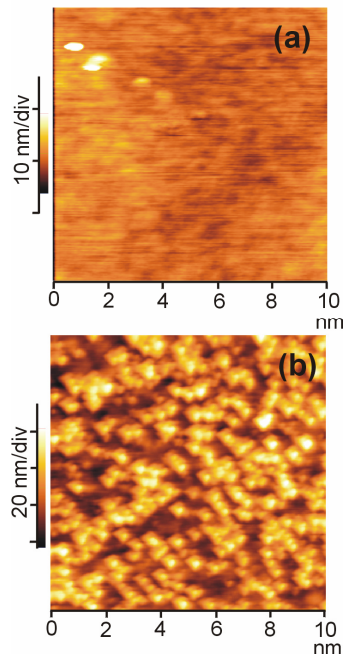


Figure 9: AFM of (a) CdSe and (b) PbSe nanoparticle films. Note the difference in vertical scales.

devices. The films appeared to be pinhole-free; however, smaller pinholes may have remained undetected because of the horizontal resolution of the AFM.

In Figure 10, the absorption spectra of an as-cast CdSe film, a sintered CdSe film, and a sintered PbSe film, as well as the external quantum efficiency (EQE) of a typical ITO/CdSe/LiF/PbSe/Al device, are shown. Using the cutoff wavelength of the CdSe absorption spectra, we can calculate a rough estimate of the bandgap of the nanoparticle film as-cast and after sintering. Nanoparticles of different sizes were used to fabricate devices. For the CdSe particles whose absorption spectra are displayed in Fig. 6 in particular, we
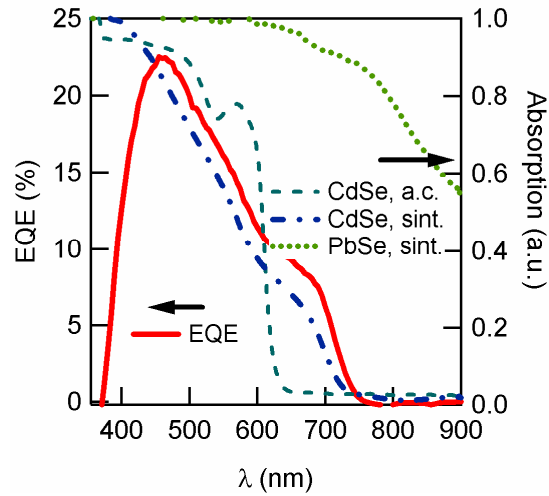


Figure 10: EQE of ITO/CdSe/LiF/PbSe/Al solar cells vs. the absorption of an as-cast (a.c.) CdSe film, a sintered (sint.) CdSe film, and a sintered PbSe film.

calculate an as-cast bandgap of around 1.97 eV (630 nm absorption cutoff) and a sintered bandgap of around 1.70 eV (730 nm absorption cutoff).

Further inspection of Figure 10 shows that the cutoff of the EQE spectrum coincides with the cutoff of the sintered CdSe film and that few photons with wavelengths above 750 nm, if any, are collected as charge at the electrodes. Because the highest excitonic peak of the PbSe nanoparticles was around 1200 nm, we expected that these solar cells would collect a portion of the infrared range of the solar spectrum. Although the EQE data may seem to suggest that the PbSe film does not play a role in these devices, other tests demonstrate the opposite. We fabricated ITO/CdSe/LiF/Al and ITO/CdSe/LiF/CdSe/Al devices, neither of which showed a photovoltaic effect. This suggests that the PbSe film is a necessary component of the system. Inspection of the current polarity showed that holes exited through the ITO and electrons exited through the top electrode. We inverted the order of the nanoparticle layers to test the ITO/PbSe/interlayer/CdSe/Al structure, with and without an interlayer. The devices showed severe shunting and no photovoltaic response, as is usually the case for CdSe/PbSe devices that do not have an interlayer.  In ITO/CdSe/interlayer/PbSe/Al devices we substituted the top Al electrode with Au, and observed somewhat lower $J_{sc}$s and FFs, but similar $V_{oc}$.

The data indicates that the main purpose of the interlayer is to interrupt shunting pathways traversing one or both nanoparticle films. This could take place by shielding the underlying CdSe layer from direct contact with the top Al electrode or by increasing the resistance of the shunted pathways in the PbSe films, which could exist along Pb-rich grain boundaries or along other inhomogeneities in the film.  In one instance alone we were able to fabricate an ITO/CdSe/PbSe/Al device with no interlayer, which yielded a $J_{sc}$ of 1.1 mA/cm$^2$, a $V_{oc}$ of 0.11 V, and a FF of 25%. This suggests that from an energy level point of view it is possible to obtain a photovoltaic effect from these devices

without the use of an interlayer; nevertheless, reproducibility was highly affected by film quality. Placed either between the nanoparticle films or above the nanoparticle bilayer, the LiF film may be further reducing leakage by passivating the nanoparticle surfaces and reducing the number of interfacial traps and recombination centers.

Finally, we consider the operational mechanism for these solar cell devices. The EQE of an ITO/CdSe/LiF/PbSe/Al device, shown in Figure 10, demonstrates that the solar cells are collecting a negligible amount of charges at photons of wavelengths above 750 nm, where the PbSe is expected to contribute. The PbSe nanoparticle films are known to be photoconductive, indicating that the PbSe does not contribute because it is energetically unfavorable for it to transfer charge to the CdSe layer. Study of the polarity of the current through these devices revealed that, strikingly, holes are collected through the ITO and electrons are collected through the top electrode.

Figure 11 shows the energy band diagram of the structure in which any possible energy level shifts due to the interlayer or to the sintering of the nanoparticle films are ignored. Although the literature provides examples in which the PbSe film is the electron transporter, the scheme in Figure 11a suggests that electrons should exit through the CdSe film. Figure 11b illustrates a possible energy diagram of the structure accounting for a decrease in the energy bandgap of the nanoparticle films once sintered. As observed by in Figure 10, the bandgap approach the bulk value when the nanoparticles are sintered at $400^{\circ}$C. Since the bandgap of bulk CdSe has a value of around 1.7 eV and the average bandgap of CdSe nanoparticles is around 2.0 eV, the change in film bandgap after sintering will have relatively minor consequences on the energy band diagram of the structure. However, an analogous change in the PbSe film could have significant consequences on the device energetics. Because PbSe has a large Bohr radius (46 nm compared to only 6 nm for CdSe) and thus shows strong quantum confinement, the difference in bandgap between bulk and nanoparticle bandgap for PbSe is large (0.27 eV vs. ~1.0 eV). As shown in Figure 11b this would cause the lowest unoccupied molecular orbital (LUMO) of the PbSe film to shift farther from vacuum and reach a value close to that of the LUMO of CdSe. To reconcile the polarity of the current with the energy levels in Figure 11b, we suggest that while electrons could travel in either the CdSe or PbSe films because of the similarity in the LUMO energies of the materials, holes may not be transferred from the PbSe to the CdSe because it is energetically unfavorable to do so. In this case, electron-hole pairs generated upon photon absorption in the PbSe film would not be collected since hole transfer to the CdSe would not occur, and thus the electron-hole pairs would ultimately recombine. Further support for this model is the observation that devices consisting of non-sintered PbSe layers did not exhibit solar cell performance.

Gur *et al.* showed that their all-inorganic nanoparticle CdTe/CdSe system behaved like a donor/acceptor type-II heterojunction. Our experiments and the literature suggest that this might not be the case for our system. The energy band diagram for our system does not present a clear scheme of staggered energy levels, so that it is not clear that we have a type-II heterojunction. Also, because the conductivity of the PbSe layer is a few orders of magnitude higher than the conductivity of the CdSe, and because we have found that the PbSe is necessary in order to collect the charge photogenerated in the CdSe, yet it does not contribute itself to the photocurrent observed, we believe this system does not behave like a typical donor-acceptor system. Instead, this system might be more similar to a $TiO_2$/conjugated polymer system in which the CdSe is the photoactive material and the PbSe acts as a low resistivity electron accepting contact.
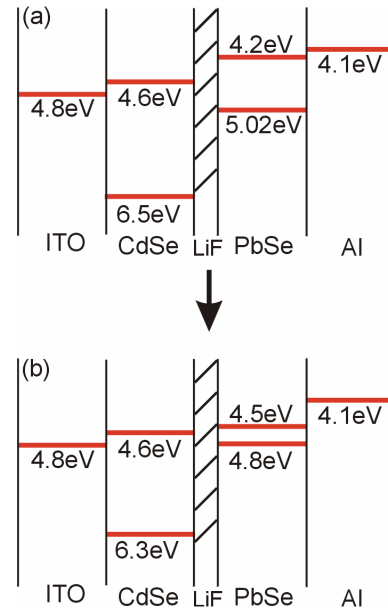


Figure 11: Possible energy band diagram for ITO/CdSe/LiF/PbSe/Al devices. Diagram (a) assumes the band gaps of the nanoparticles are not affected by sintering. Diagram (b) assumes that the band gaps decrease to the bulk value.

Finally, we considered whether the ITO/CdSe/(interlayer)/PbSe/Al could be behaving like a p-n junction system. Because CdSe is an n-type material, electron transport by the PbSe film would have had to stem from an even stronger n-type doping of the PbSe. The literature on PbSe thin films indicates that photoconductivity in this material, which we observed and presented in Fig. 5, is possible when oxygen impurities introduce acceptor levels into the energy band of PbSe, making it p-type. While it may not be entirely correct to apply literature on semiconductor thin films, which is mostly based on mono- or polycrystalline systems, to nanoparticle solids, we found the data in the literature to be irreconcilable with our observations of the photoconductivity and electron conduction in PbSe.

## $Cd_xHg_{1-x}Te$ nanoparticle solar cells

When Hg is doped into CdTe to form the ternary compound $Cd_xHg_{1-x}Te$, the absorption spectrum is shifted past the CdTe absorption edge of 850nm and into the near-IR. The amount of incorporated Hg determines the energy level shift, allowing one to tune the bandgap by controlling the doping level. With a tunable band-gap going into the near-IR, CdHgTe allows one to construct a bulk-material-based solar cell with performance in our target range of $\lambda > 750nm$. Literature reports have demonstrated that $Cd_xHg_{1-x}Te$ can be used in place of CdTe in a CdS/CdTe heterojunction device, with many of the known CdTe device processing steps being applicable for the $Cd_xHg_{1-x}Te$ device.

For these reasons, we investigated the synthesis of $Cd_xHg_{1-x}Te$ nanoparticles to be incorporated into $Cd_xHg_{1-x}Te$ / CdSe sintered devices, a design analogous to a CdTe / CdSe solar cell presented in the literature and further explored by our group.

For initial trials, devices with the structure $Cd_xHg_{1-x}Te$ / CdSe were fabricated under low processing temperatures of 220C, without a high-temperature $CdCl_2$ treatment to promote grain growth and improve PV performance, in order to minimize disruption to the film quality. Results up to $J_{sc}$=1.4mA/cm2, $V_{oc}$=-0.1V and ff=28% were obtained, as shown in Figure 12. Comparison with the dark currents showed that shunting was a major loss mechanism; likely due to physical defects in the film. External quantum efficiency measurements (Figure 13) showed that although the efficiency was low across the wavelength range, the photocurrent generation did extended up to at least 900nm, thus demonstrating an all-inorganic nanoparticle device with performance extended into the near-IR. At the time of this measurement, the range of our EQE system was limited to a maximum of 900nm. Improved performance was expected for device receiving a $CdCl_2$ treatment at temperatures elevated to 400C.
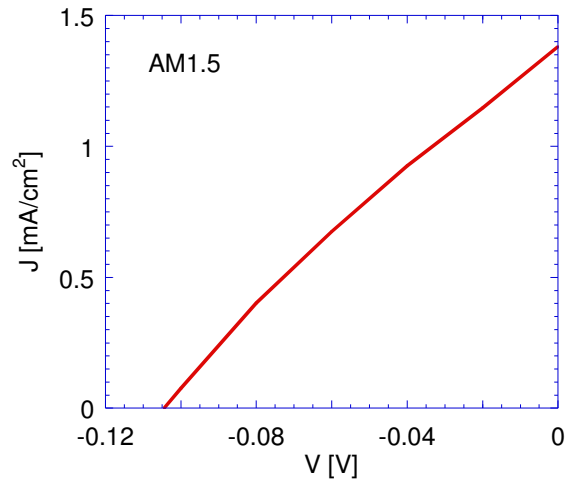


Figure 12: J-V characteristic for an ITO / $Cd_xHg_{1-x}Te$ / CdSe / Al device processed at only 220C with no $CdCl_2$ treatment.
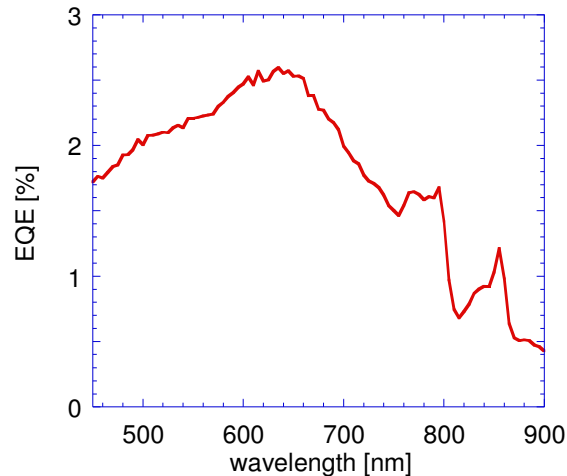


Figure 13: External quantum efficiency *vs.* wavelength for the ITO / $Cd_xHg_{1-x}Te$ / CdSe / Al device of Figure 12.

Difficulties were encountered while pursuing further development work on the $Cd_xHg_{1-x}Te$ sintered devices, as the Hg doping level in the $Cd_xHg_{1-x}Te$ nanoparticles proved to be challenging to control. One series of experiments indicated a higher percentage of Hg incorporation than anticipated, as characterized by energy dispersive spectroscopy (EDS), though it should be noted that this measurement technique is spatially limited to a small area <1µm and may not be representative of the material as a whole. Rather than completely incorporating as an alloy, CdTe and HgTe might have formed separate phases resulting in an inhomogeneous blend, with some areas more Hg-rich than others. Sintered devices made using this batch of material yielded no photovoltaic response. In response to this, efforts were pursued to more stringently limit the amount of Hg exchange during synthesis, resulting in particles with 40% Hg inclusion ($Cd_{0.6}Hg_{0.4}Te$) as characterized by Direct Couple Plasma (DCP). Devices of the type ITO/ $Cd_xHg_{1-x}Te$ / CdSe / Al were made from this material, with processing including a 400C $CdCl_2$ sinter treatment. This resulted in functional solar cell devices (Figure 14), but absorption spectra of the sintered films did not show a band-gap decrease compared to CdTe and external quantum efficiency measurements of the devices did not yield photocurrent production above the 850nm cut-off value displayed in analogous CdTe devices (Figure 15).  We consider three possible theories to explain this scenario: a) alloyed $Cd_xHg_{1-x}Te$ particles with an even distribution of Hg throughout the particle volume were made, but for some reason the Hg migrated outside of the particle during the high temperature $CdCl_2$ sintering process; b) inclusion of Hg in the CdTe took the form of a core-shell structure rather than a uniform alloy; c) HgTe particles were formed as separate entities rather than Hg being incorporated inside the CdTe particles. Each of these theories could result in spatially separated HgTe and CdTe domains. Further material characterization, especially of the sintered nanoparticle films, is required in order to understand what is happening and to correct the deficiency which limited the spectral performance of this material from expanding into the near-IR.
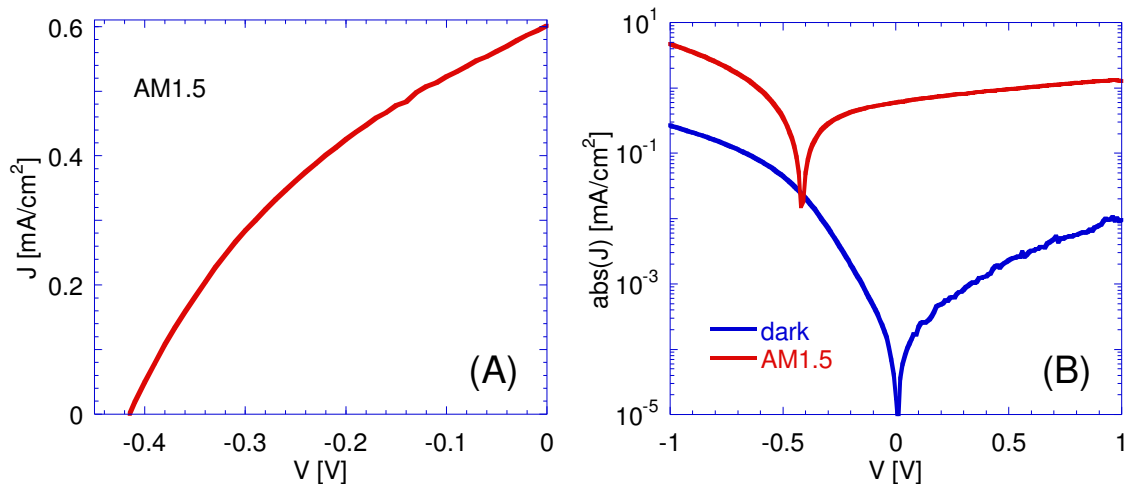


Figure 14: ITO/ $Cd_{0.6}Hg_{0.4}Te$/CdSe/Al device data: (A) under AM1.5 and (B) comparing dark to AM1.5 on a semi-log scale.
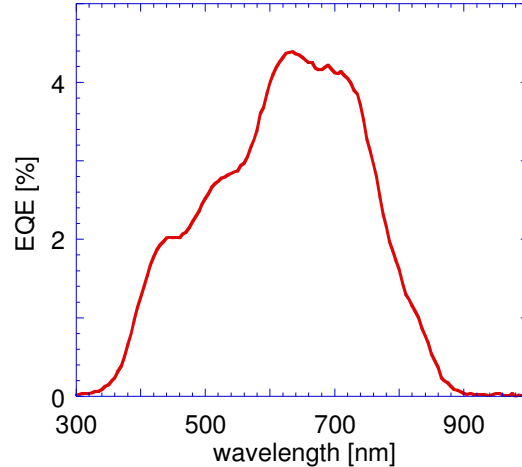
Figure 15: External quantum efficiency spectra for an ITO/ $Cd_{0.6}Hg_{0.4}Te$/CdSe/Al sintered device.

A secondary approach to creating $Cd_xHg_{1-x}Te$ films was employed, involving the separate synthesis of both CdTe and HgTe nanoparticles and subsequently sintering films deposited from a 1:1 blend of the two constituents. Absorption spectra of the resultant films showed a characteristic similar to that of pure CdTe, with no absorption extended past 850nm.

Our earlier results, though having low device efficiency, demonstrated photocurrent generation past 850nm and into the near-IR, showing that $Cd_xHg_{1-x}Te$ nanoparticle solar cells are a viable approach for an all-inorganic nanoparticle solar cell functioning in the IR. However, further pursuit to understand the nature of the particles and sintered $Cd_xHg_{1-x}Te$ films was cut short by the end of our Phase I award period.


**Quantum-confined nanoparticle solar cells**

Our CdSe/PbSe sintered nanoparticle device experiments demonstrated that the sintered PbSe films did not contribute to photocurrent generation, a fact which we attributed in part to the small 0.28 eV band-gap of bulk PbSe. To address this issue, PbSe and HgTe nanoparticles were investigated as IR-absorbers in non-sintered devices which retained the quantum-confined behavior of the particles and hence provided a comparatively increased band-gap. PbSe particles with a band-gap of $E_g$~0.82 eV and HgTe particles of $E_g$~0.90eV were used for these experiments. A variety of Schottky-junction as well as donor and acceptor heterojunction partner bilayer device designs were construction.  Acceptor materials included both sintered CdSe and $TiO_2$ nanoparticle layers, as well as CdS deposited by chemical bath deposition. Donor materials were represented by sintered CdTe nanorod films. Single layer Schottky-junction devices utilized Ca and Al electrodes. Table 1 summarizes the various device structures investigated in this part of the work. Constraints against heating the PbSe and HgTe films (to maintain quantum-confined behavior) and requirements for working in the inert atmosphere glovebox guided device designs such that the bilayer partners (either high

temperature sintered or chemical bath deposited films) had to be deposited prior to PbSe or HgTe layers.

| | bilayer partner | PbSe | HgTe |
|---|---|---|---|
| **Bilayer devices** | **CdSe** | ITO / CdSe / PbSe / Au | ITO / CdSe / HgTe / Au |
| | | ITO / CdSe / PbSe / Al | |
| | **CdS** | ITO / CdS  / PbSe / Au | ITO / CdS / HgTe / Au |
| | | ITO / CdS  / PbSe / Al | |
| | **CdTe** | ITO / CdTe / PbSe / Al | ITO / CdTe / HgTe / Al |
| | **TiO$_2$** | | ITO / TiO$_2$ / HgTe / Au |
| **Schottky devices** | | ITO / PbSe / Ca / Al | |
| | | ITO / PbSe / Al | |

Table 1: Device structures investigated for PbSe and HgTe quantum-confined, non-sintered nanoparticle devices.

PbSe and HgTe nanoparticle layers were deposited via a layer-by-layer dip-coating process. An in-film exchange of the native ligand on the nanoparticle for a less soluble ligand allowed for multiple coating depositions without removing the prior nanoparticle layers. The exchange ligand has the added benefit of promoting improved charge transport, as it is smaller than the original more bulky ligands and leads to short inter-particle distance, and hence better conductivity, while retaining the quantum-confined characteristics of the material.

Various in-film ligand exchange treatments have been discussed in the literature, including hydrazine, pyridine, methlamine and ethanedithiol (EDT). For our work, we used a 0.1M EDT solution in acetonitrile (ACN). All PbSe and HgTe film work, from fabrication through device testing, was performed under inert atmosphere to avoid oxidation of the nanoparticle surface. Substrates were dipped in a dilute 5 mg/ml nanoparticle solution, where the solvent was a chloroform:hexane blend. The substrates were removed from solution at a rate of 0.1-0.2 inches/second, leaving behind a monolayer of nanoparticles. After air drying, the film was dipped in the EDT solution for 3-5 seconds to exchange EDT for the native ligand, removed and then rinsed with ACN and blown dry. Repetition of this process anywhere from 20-40 times yielded shiny films ranging from 100-200nm in thickness. Characterization of the surface topology with AFM showed smooth films with a surface roughness on the order of $R_a$=1nm for a typical PbSe film (Figure 16A) . Cross section SEM (Figure 16B) confirmed the films were continuous and dense. Shiny films were also obtained for HgTe, though the surface roughness increased slightly to $R_a$=7nm.
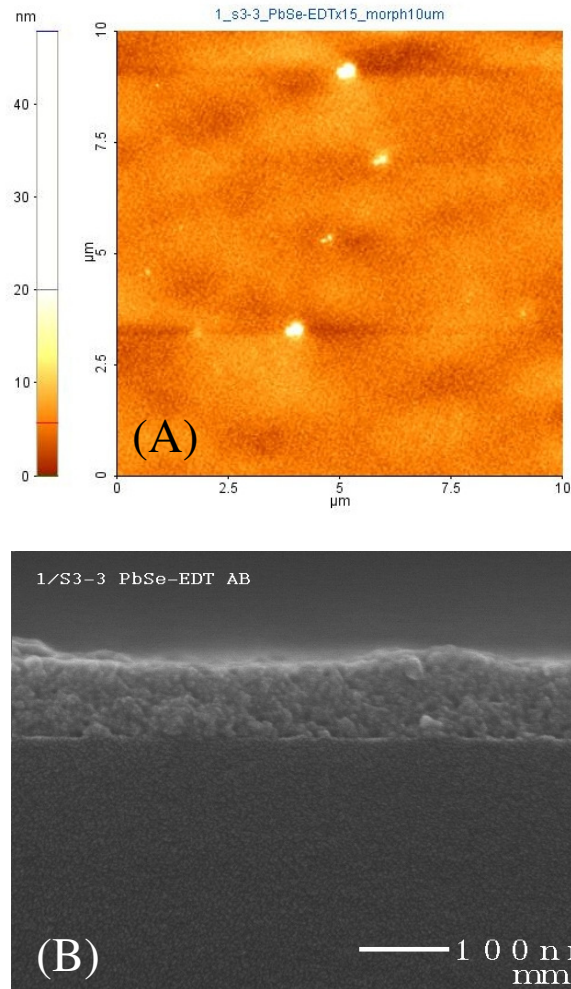
Figure 16: (A) AFM surface topology of a layer-by-layer deposited PbSe; (B) cross-sectional SEM of the same film.

CdTe and CdSe films were spin-cast from nanoparticle solutions and sintered at 400C in either inert (CdTe) or ambient (CdSe) atmosphere for 15 minutes. CdS was deposited by chemical bath deposition and receive no further treatment prior to the absorber layer deposition. Electrodes were thermally evaporated in a chamber inside the glovebox so that the PbSe and HgTe films were not exposed to oxygen.

*PbSe quantum-confined nanoparticle devices*

The PbSe layers did not demonstrate photocurrent generation in any of the bilayer or Schottky-junction devices explored during this award. In the case of the Schottky and the CdTe/PbSe structures, devices did not produce any photocurrent or photovoltage. The CdSe/PbSe structures produced working solar cell devices, but as illustrated in Figure 17B for the CdSe/PbSe, a comparison of the EQE with the absorption spectra of the individual films shows that photocurrent was produced in the CdSe with no contribution

from the PbSe. The photocurrent spectral range matches that of CdSe absorption, showing no photocurrent generation above the CdSe 750nm band-edge.

Investigations completed after the end of this grant solved the mystery of why the quantum-confined PbSe was not photoactive. The band-gap requirements for PbSe to contribute photocurrent are apparently even more restrictive than we initially assumed. Decreasing the particle size and subsequently increasing the bandgap to a value of 1.0 eV yielded photocurrent producing PbSe thin film devices.
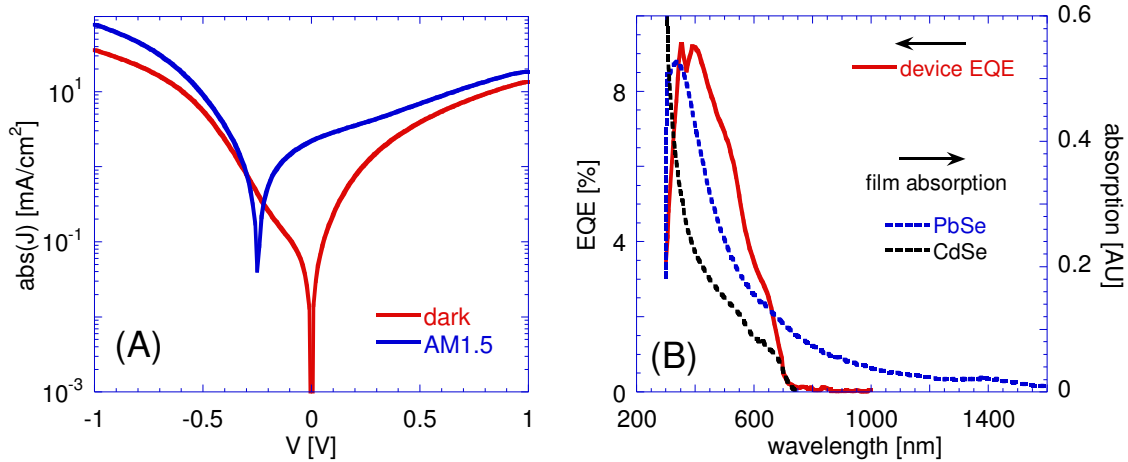


Figure 17: (A) J-V results for an ITO/CdSe/PbSe/Al device producing $J_{sc}$=2.2mA/cm2, $V_{oc}$=-0.25V and ff=29%; (B) EQE for an ITO/CdSe/PbSe/Au device, with the absorption spectra of CdSe and PbSe films plotted for comparison.

*HgTe quantum-confined nanoparticle devices*

The HgTe bilayer devices did produce photocurrent created in the HgTe layer when paired with CdS, CdSe or TiO$_2$. The ITO / CdS / HgTe / Au device shown in Figure 18A achieved $J_{sc}$=11mA/cm2, $V_{oc}$=-0.17V and ff=23%. The HgTe contribution to the photocurrent was most evident in the CdS/HgTe and TiO$_2$/HgTe devices, where the absorption range of the partner material was either limited to lower wavelengths (CdS) or the material was mostly transparent in the visible range (TiO$_2$). Figure 18B plots the CdS / HgTe device EQE alongside the CdS and HgTe film absorption. The EQE magnitude is highest below 520nm, but it does extend up to 800nm. As can be seen from the band-edge of CdS, photocurrent produced above 520nm must be originating from the HgTe absorption. However, though HgTe absorption extends past 1500nm, the absorption strength is maximized in the visible range below 600nm. As a result, the HgTe devices produced insufficient photocurrent in the near-IR to meet our objectives. From this experiment, we learned an important criterion for IR-solar cell material selection. Though a variety of nanoparticles exhibit absorption throughout the near-IR, and are often touted as attractive IR-absorbers with adjustable bandgaps, such characteristics are not a sufficient condition for the production of solar cells with decent efficiency in that region of the spectrum. For planar device designs, it is also required that the absorption coefficient has a high value in the region of interest in order to absorb enough light to produce a photocurrent sufficient for high performance. While some of this issue can be addressed by increasing the thickness of the absorber layer, this can only be adjusted to a

certain point before charge transport losses begin to have a negative impact on performance.
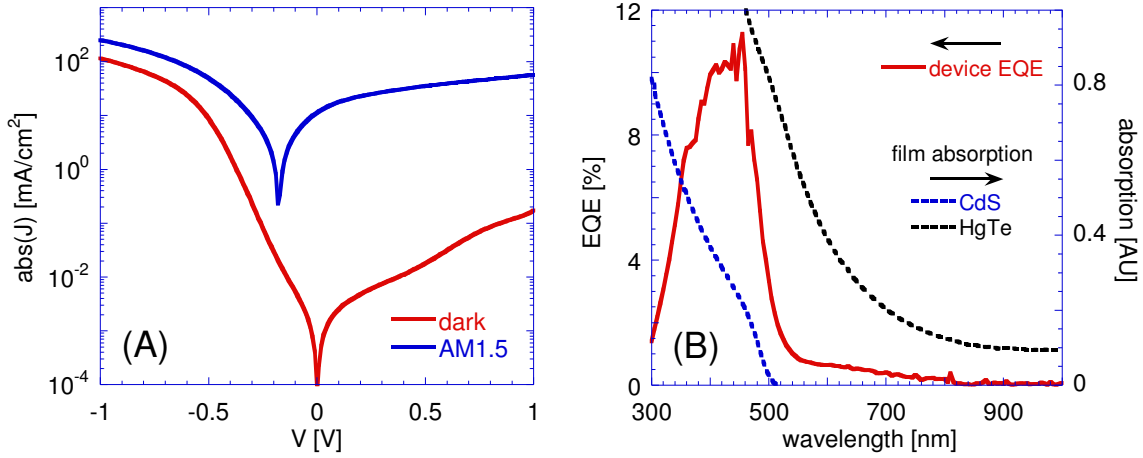


Figure 18: ITO / CdS / HgTe / Au device results: (A) J-V curves in the dark and under AM1.5; (B) EQE with the absorption spectra of CdS and HgTe films plotted for comparison.

## CdTe / CdSe sintered nanoparticle devices

The CdTe / CdSe device system was used as a vehicle to expand our general understanding of all-inorganic nanoparticle solar cell physics. Additionally, it was anticipated that the knowledge gained from studying this system would be directly applicable to understanding and improving the $Cd_xHg_{1-x}Te$ / CdSe devices discussed above. We fabricated ITO/CdTe/CdSe/Al solar cells with a short-circuit current of 18.7 $mA/cm^2$, an open-circuit voltage of 0.404 V, and a fill factor of 34%, yielding a power efficiency of 2.6%. This result exceeds the efficiency reported by Gur et al. for Al electrodes, without the need for an additional atomic layer deposited $Al_2O_3$ layer. The CdTe/CdSe devices were shown to contribute to the quantum efficiency out-to to 900 nm. We studied a wider variety of electrodes and demonstrated that the electrode selection, with the exception of PEDOT-PSS, did not substantially affect the device performance. We also studied the sintering conditions and showed the devices are highly sensitive to sintering temperature, indicating that the optimization of the sintering conditions, as well as interface layers, will be the best route to significantly improve device efficiency. Finally, we measured the temperature dependence of an all-inorganic nanoparticle solar cell for the first time, and demonstrated that $J_{sc}$ increases with increasing temperature while $V_{oc}$ decrease with increasing temperature. This behavior is reminiscent of polymer-nanoparticle donor-acceptor heterojunctions or Schottky devices, rather than p-n junction devices. A paper on these results is currently being written.

The fabrication of CdTe/CdSe devices was similar to the process used to fabricate the CdTe/PbSe solar cells, with nanorods replacing the nanoparticle form for CdSe. Devices were fabricated by spin coating CdTe and then CdSe on a patterned ITO substrate and annealing at 215-220C between layers. Prior to electrode deposition, the device was treated with $CdCl_2$ in methanol and then sintered in air at 400C in a standard single-zone tube furnace. A variety of electrodes, including Ca, LiF, Al, and Au were



Figure 19: ITO/CdTe/CdSe/Al solar cell with a power efficiency >2.5%.

deposited by thermal evaporation while PEDOT-PPS was deposited by spin casting. A typical IV-curve for one of the better devices is shown in Figure 19. While $J_{sc}$ above 15 mA/cm$^2$ was observed on several different batch runs at both UCSC and Solexant, currents of ~3 to 5 mA/cm$^2$ were more typical. The difference in the currents was related to differences in the nanoparticle solutions, particularly with aging, as well as the sintering conditions. What synthesis conditions result in the best device performance is still under investigation.
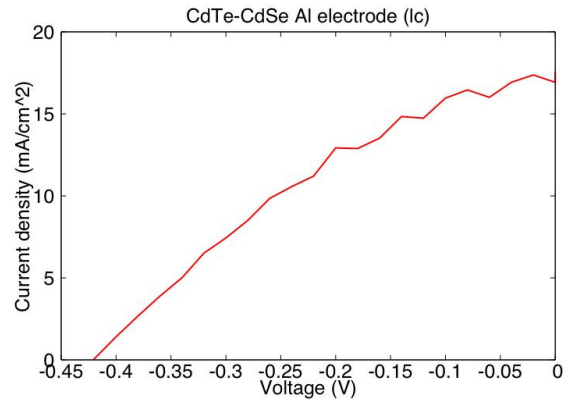
In Figure 20a, the performance for an unsintered device is shown, revealing a large reduction in $J_{sc}$, and a significant variation in $J_{sc}$ was also observed with changes in the annealing temperatures as small as 10 degree (Figure 20b). Given that the single zone furnace we used has a variation of over 10 degrees in its temperature uniformity, more control over the temperature, as afforded by a three zone furnace, is required for device optimization and reproducibility.
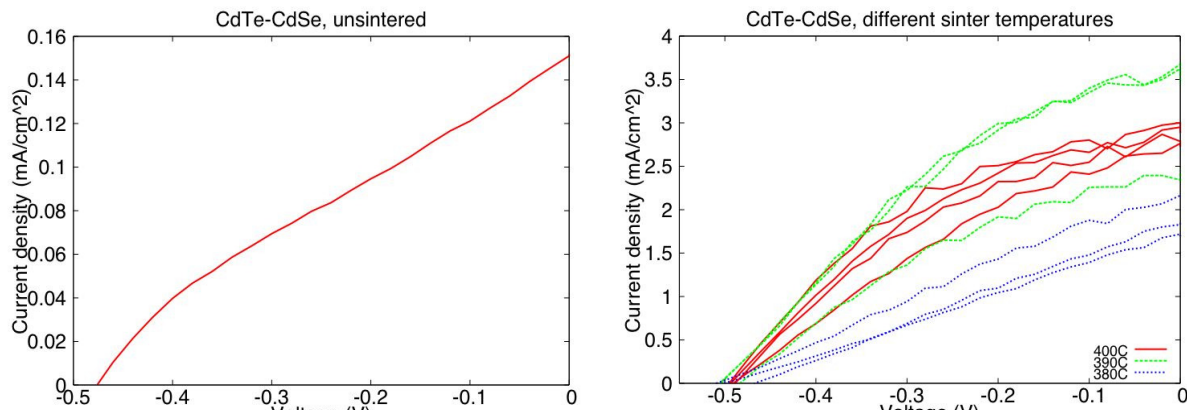


Figure 20: Typical performance of an ITO/CdTe/CdSe/Al solar cell that has been (a) unsintered, and (b) sintered at different temperatures, 380 to 400 C.

We tested the effect of several different electrodes, including Au, PEDOT/Au, Al, Ca, and LiF/Al. In general, the CdTe/CdSe devices are insensitive to choice of electrodes. In Figure 21, the effect of Al and Au electrodes on device performance is shown for CdTe/CdSe and for CdS/CdTe for comparison purposes. The only substantial

electrode dependence for CdTe/CdSe devices was observed when PEDOT-PPS was spun-cast between the CdSe and Au interface, resulting in very low $V_{oc}$. In contrast, CdS (deposited by chemical bath deposition) and CdTe nanoparticle devices showed strong electrode dependence, with the largest $V_{oc}$ occurring for PEDOT-PSS electrodes. This indicated that these devices operate by fundamentally different mechanisms. We further note that the typical device performance is very similar for the CdS/CdTe vs. CdSe/CdTe devices, further suggesting that the CdTe material and the sintering conditions may be the limiting factor controlling device performance for both systems.

  Approaches to further improve device performance are suggested by cross-sectional SEM (taken at the Molecular Foundry in Berkeley). In Figure 22, typical SEMs are shown for a sintered CdTe/CdSe bilayer on a silicon

Figure 21: The effect of device performance on electrodes for (a) CdTe/CdSe and (b) CdS/CdTe.

substrate. The CdTe layer forms grains on the order of 10 nm in diameter while the thin CdSe layer forms a more columnar structure oriented normal to the substrate. Large voids are frequently observed, particularly at the CdSe/CdTe interface, indicating that improvement to this interface will be needed for better device performance. In addition, more crystallinity of the CdTe layer will be needed to increase mobility and ultimately $J_{sc}$ and the fill factor.
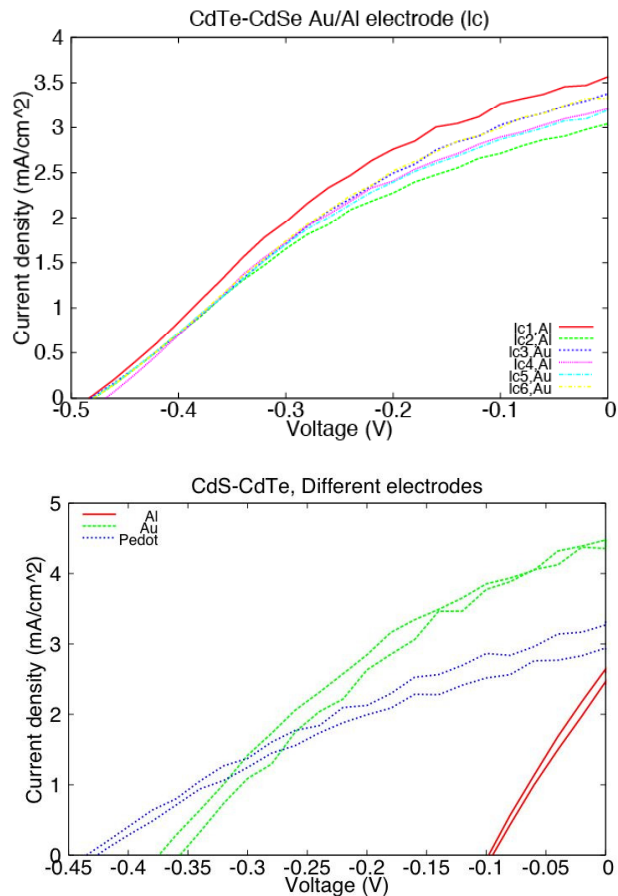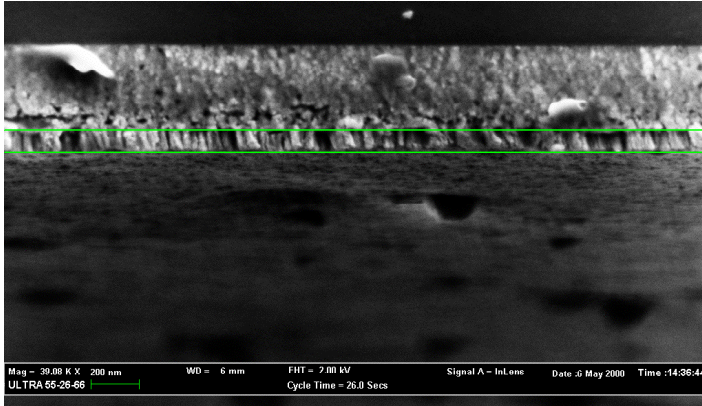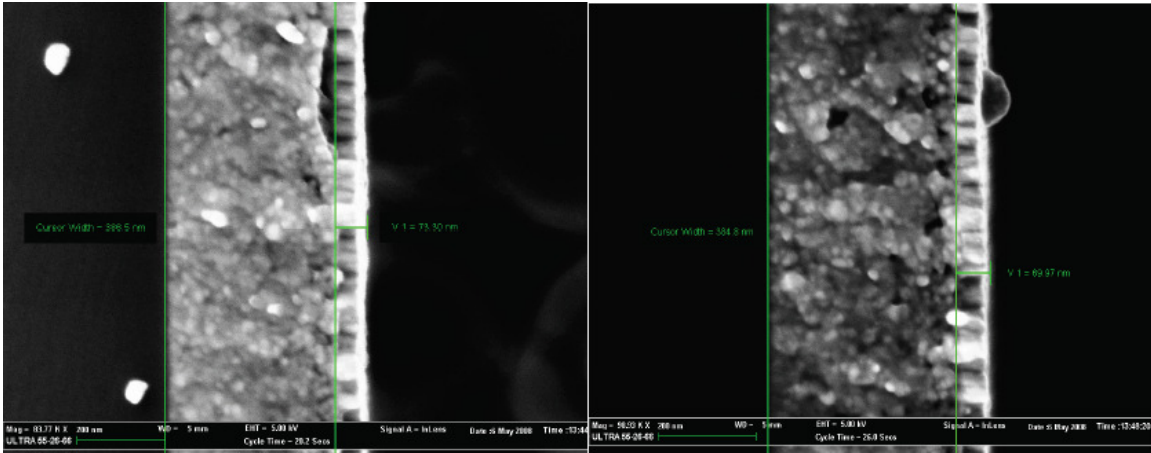
Figure 22: SEM cross sections of a sintered CdTe (~400nm), CdSe (~100 nm) bilayer, revealing the different grain structure and presence of voids at the CdTe/CdSe interface.

The temperature dependence of a typical CdTe/CdSe device is shown in Figure 23. Remarkably, a very strong T-dependence for both $V_{oc}$ and $J_{sc}$ is observed. The $J_{sc}$ drops by a factor of 4 and the $V_{oc}$ more than doubles between 350K and 100K. The $V_{oc}$ reaches 0.85V at 100K, suggesting that substantial improvements can be made. Surprisingly, the temperature dependence of the CdSe:P3HT blends is similar, although not as strong, as the all inorganic CdTe/CdSe devices. This result could indicate that transport in the CdTe is dominated by hopping, as is the case for the P3HT polymer. Alternatively, the decrease in $J_{sc}$ with decreasing temperature may be indicative of a Schottky barrier play an important role in the device performance.
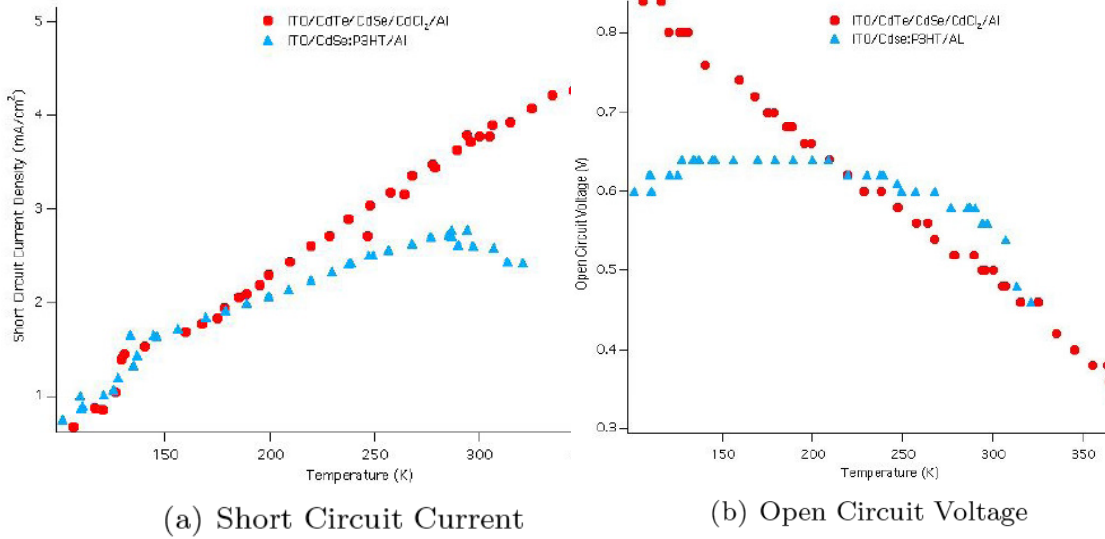
(a) Short Circuit Current  (b) Open Circuit Voltage

Figure 23: The temperature dependence for sintered ITO/CdT/CdSe/Al and ITO/CdSe:P3HT blend for comparison, showing (a) $J_{sc}$ and (b) $V_{oc}$

Changes in the absorption before and after sintering (Figure 24b) reveal a shift towards bulk behavior due to loss of quantum confinement of the nanoparticles. The onset of the absorption (and quantum efficiency) is on the order of 840 nm, which is near the 1.5 eV bulk bandgap for CdTe. The fall off in absorption and quantum efficiency at shorter wavelengths is due to absorption by the substrate (quartz and glass, respectively). Curiously, the external quantum efficiency, shown in Figure 24b, appears to start at close to ~900 nm which is below the bandgap of pure CdTe. This suggests that interface doping or defect states in the gap are contributing to the short circuit current. Overall, a peak external quantum efficiency near 50% is observed for the better devices. An appreciable quantum efficiency of up to 30% is still observed in the IR region between 700 and 900 nm; however this
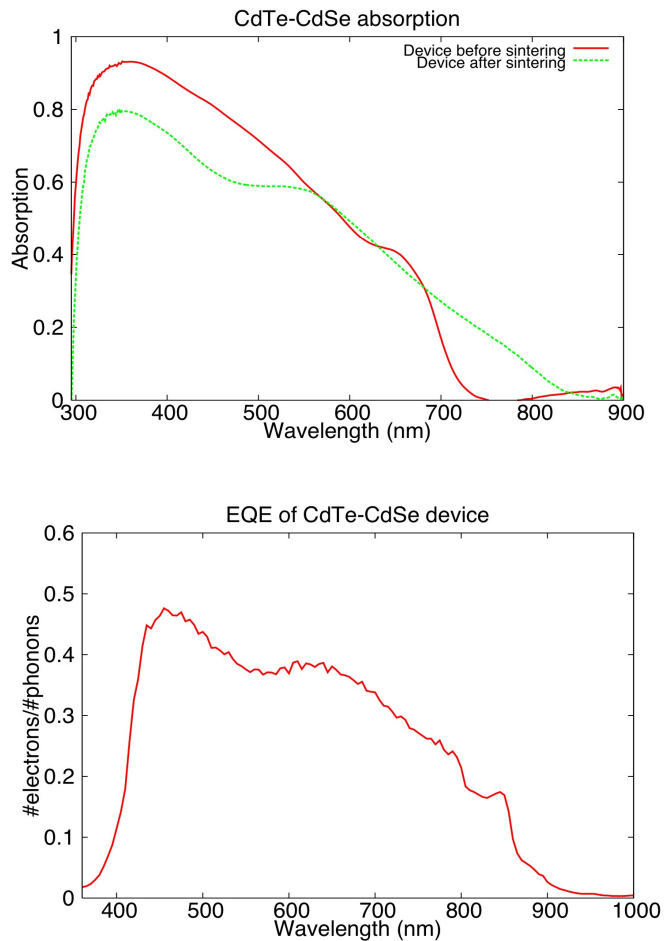


Figure 24: Top: absorption of a sintered and nonsintered CdTe/CdSe. Bottom: External quantum efficiency of a sintered CdTe/CdSe device.

still results in a power efficiency less than 1% in the near-IR for the best-device.

## *Conclusions*

Though the performance of the devices generated under this grant were less than originally predicted at the outset of the study, we believe that the work completed under this award offers strong insight into viable avenues of research for this area in the future.

We presented proof-of-concept results demonstrating that non-sintered $Cd_xHg_{1-x}Te$ nanoparticle devices represent one such pathway towards achieving solar cell performance in the near-IR wavelength regime. Further work to characterize the material properties of the sintered films is required in order to proceed with this research, but once that issue is solved, the $Cd_xHg_{1-x}Te$ system is very promising.

Other research completed over the course of this award has given greater insight into the criteria necessary to produce a functional quantum-confined nanoparticle-based solar cell with efficient performance in the near-IR. Material band-gap was demonstrated to be a crucial factor for PbSe devices, where changing the band-gap from 0.8 to 1.0eV made the difference between non-functional and functional PbSe films. In the case of Hg devices, the absorption strength of the material as a function of wavelength was shown to be just as important as the absorption range in general. It is not sufficient to select a material which absorbs in the near-IR – it must absorb strongly in that range.

While we did not observe a near-IR response for the CdSe/PbSe devices, our work revealed the important role that buffer layers play in reducing shorting and improving device performance for all inorganic nanoparticle solar cells. Further control over the interfaces using buffer layers will likely play as valuable a role for nanoparticle solar cells as it does for thin film solar cells.

Finally, our ability to further improve on CdTe/CdSe nanoparticle solar cells by eliminating the need of an ALD $Al_2O_3$ layer or Ca electrode and to further elucidate the mechanisms that will be responsible to improve device performance will be extremely valuable for producing a commercially viable nanoparticle solar cell. Although our goal was to study CdTe/CdSe as a model system to understand nanoparticle solar cells, and not to obtain a large IR response, we still observed one of the highest near-IR quantum efficiencies every observed in a nanoparticle-based solar cells. This promising result suggests that just minor doping of the CdTe layer will be sufficient to harness a substantial fraction of the near-IR spectrum.

All-inorganic nanoparticle-based solar cells are a very new field, but they offer numerous advantages including ease of tuning the material properties via control of material synthesis, the economical fabrication of solution-processing deposition and likely a system less vulnerable to degradation than their counterpart solution-processed organic photovoltaic materials.